

# Mechanism of droplets on electrowetting-on-dielectric chips transition from stillness to motion

X Xu<sup>1,2\*</sup>, Y Zhang<sup>1,2</sup> and L Sun<sup>3</sup>

<sup>1</sup>College of Mechanical Engineering, Quzhou University, Quzhou 324000, China

<sup>2</sup>Key Laboratory of Air-Driven Equipment Technology of Zhejiang Province, Quzhou University, Quzhou 324000, China

<sup>3</sup>Robotics and Microsystem Center and Collaborative Innovation Center of Suzhou Nano Science and Technology, Soochow University, Suzhou 215001, China

Received: 09 January 2018 / Accepted: 24 July 2018 / Published online: 13 October 2018

**Abstract:** Digital microfluidics technology based on the electrowetting-on-dielectric effect is a popular emerging technology whose objects of control are individual droplets on the microliter or even nano-liter scales. It has unique advantages such as rapid response, low reagent consumption, and high integration, so it has drawn widespread attention and use in the biological, medical, and chemical fields. However, to date, there has been relatively little research conducted on the mechanism of droplets transition from stillness to motion by electrowetting-on-dielectric actuation. Here, we studied the polarization mechanism underlying solid–liquid contact surface, thus building upon the previous research. The electric field in chip, internal pressure, and flow field of droplet were modeled and simulated numerically. Then, the process and mechanism of droplet transition from stillness to motion was comprehensively analyzed, and the results obtained from the simulation and discussion were in close agreement with experimental results. It is here shown that the process of droplet from stillness to motion involves four successive steps, which helps to better understand electrowetting-on-dielectric-induced droplet motions and physics of digital microfluidics systems. The aim of this work was to research basic physical mechanisms of electrowetting-on-dielectric droplet motion on a common ground so that the researchers may form a clear picture of the fundamentals.

**Keywords:** Digital microfluidics; Electrowetting-on-dielectric; Droplet motion; Hydrostatic pressure; Driving mechanism

**PACS Nos.:** 47.55.D–; 68.03.Hj; 68.03.Cd; 77.22.Ej

## 1. Introduction

In recent years, the rapid development of micro-fabrication processes has brought considerable breakthroughs and improvements to microfluidics technology. Taking advantage of electrowetting-on-dielectric (EWOD) mechanism has become a trend in microfluidics [1–6]. The current technique for manipulating droplets based on the EWOD mechanism is known as digital microfluidics [7–12]. It has four basic controls: the generation of droplets from a reservoir, the division of one droplet into two sub-droplets, the merging of two droplets into one droplet, and the transportation of droplets [13–23]. Digital microfluidics

technology does not require complex mechanical compartments such as micropumps, microvalves, and microbubbles, thus avoiding any need for the manufacturing or assembly of complex parts, contamination from different liquids, or flow blockage. The digital microfluidics chip can control a single microdroplet of microliter or nano-liter size, enabling its widespread use in “lab-on-a-chip” systems [24–26]. The substances contained in the droplets require little time to react, and the reaction is very thorough. The droplets can contain cells, DNA, protein, enzymes, antibodies, embryos, and other substances [27–35]. Digital microfluidics technology has broad applications in other fields, such as optics [36], chip cooling [37], and sensors [38].

In digital microfluidics technology, the movement of droplet takes place within an electric field under the action

\*Corresponding author, E-mail: 851597503@qq.com

of a series of mechanisms [39–43]. The mechanism includes processes that take place across multiple scales and stages [44–46]. A review of relevant studies performed by other researchers shows that various hypotheses have been proposed for the mechanism underlying the movement of droplets on EWOD chips. Among the reviewed studies, notable examples include the work by Walker et al. [14] who presented a distributed parameter model of EWOD fluid dynamics that was able to approximately capture the evolution of a droplet’s liquid–gas interface by means of the level set method in two dimensions. Starting from the full Navier–Stokes equations, a reduced order model was established, similar to Hele–Shaw-type flow including the relevant boundary phenomena, that the bulk dynamic behavior of EWOD-driven droplets in two dimensions was captured. In addition, Lee et al. [47] visualized the flow pattern and measured the flow velocity within the droplet. The experimental results were compared to numerical results and the two showed qualitative agreement, which indicated that the flow observed during high-frequency voltage EWOD was caused mainly by the electrothermal effect, in which the electrical charges were induced by conductivity and permittivity gradients. Furthermore, Schertzer et al. [48] demonstrated some analytical models that describe the capillary force on confined droplets actuated in EWOD devices and the reduction in that force by contact angle hysteresis as a function of the three-dimensional shape of the droplet interface. These models were used to develop an analytical model for the transient position and velocity of the droplet. Similarly, Cui et al. [49] proposed a dynamic saturation model of droplet motion on the single-plate EWOD device. The phenomenon that droplet velocity is limited by a dynamic saturation effect was precisely predicted. Their work presented the relationship between dynamics of electrowetting-induced droplet motion and device physics including device structure, surface material, and interface electronics. Chatterjee et al. [41] presented a general electromechanical model for calculating the forces on insulating and conducting liquids in two-plate devices. The model revealed not only the relative ease in which liquids of different polarities and conductivities can be actuated, but also the contributions of electrowetting and dielectrophoretic forces to droplet actuation in a two-plate digital microfluidics system. Ahmadi et al. [20] developed a model for microdroplet motion and dynamics in contemporary electrocapillary-based digital microfluidics systems. The proposed pseudo-three-dimensional approach provided an efficient and accurate tool for modeling the microdroplet dynamics which decreased the computation time drastically. Nelson et al. [50] explained the theoretical progression from electrocapillarity to the electrowetting equation and summarized the development of the basic EWOD technologies

and then discussed the basic physics of EWOD and explained the mechanical response of a droplet using free-body diagrams encompassing all the existing interpretations. Combined with the works mentioned above, in order to strengthen the understanding and also reveal the droplet transition mechanism, in this work, the process and mechanism underlying the transition of droplets from stillness to motion was based on the previous research and performed through theoretical analysis and numerical simulation. First, we established the polarization mechanism underlying solid–liquid contact surface in EWOD device, thus building upon the previous research. Additionally, the electric field in the chip, internal pressure, and flow field of droplet were modeled and simulated numerically. Further, experiments were carried out to study and analyze the droplet transport motion. We here observed that the droplet can be driven by a sufficient difference in hydrostatic pressure. From this, it can be seen that the transition of droplets from stillness to motion involves four successive steps. This work focuses on the fundamentals of how droplets move from stillness to motion by EWOD actuation. The primary objective of this paper is to provide a theoretical basis for a better understanding and use of digital microfluidics technology.

## 2. Brief review from electrocapillarity to electrowetting-on-dielectric equation

In electrocapillarity and electrowetting, the driving electrode and the conductive liquid are in direct contact, so the Helmholtz capacitance per unit area of solid–liquid interface (electrical double layer, EDL)  $c_H$  can be expressed as follows [51]:

$$c_H = \frac{\varepsilon_0 \varepsilon_r}{\lambda_D}, \quad (1)$$

Here,  $\varepsilon_0$  and  $\varepsilon_r$  represent the permittivity of vacuum and the relative dielectric constant of conductive droplet, respectively.  $\lambda_D$  represents the Debye-screening length. It is usually a few nanometers in size. The relationship between the added voltage in the electrocapillary and solid–liquid interfacial tension can be expressed by Lippmann equation [52]:

$$\gamma_{sl} = \gamma_{sl,0} + \frac{1}{2} c_H V^2, \quad (2)$$

Here,  $\gamma_{sl,0}$  is the solid–liquid surface tension without driving voltage,  $V$  here is voltage drop across EDL, and the three-phase contact line tension can be expressed using Young’s equation:

$$\gamma_{sl} = \gamma_{sg} - \gamma_{lg} \cdot \cos \theta, \quad (3)$$

Here,  $\theta$  represents the droplet contact angle.  $\gamma_{lg}$  and  $\gamma_{sg}$  represent the gas–liquid surface tension and the solid–gas surface tension, respectively, and whose value remains constant. So, Young’s equation can be used to represent the change of the contact angle in Lippmann equation, and the Young–Lippmann equation can be obtained as follows:

$$\cos \theta_V = \cos \theta_0 + \frac{1}{\gamma_{lg}} \cdot \frac{1}{2} c_H V^2, \quad (4)$$

Here,  $\theta_V$  and  $\theta_0$  represent the contact angle in the presence of driving voltage and the initial contact angle, respectively. Accordingly, the dimensionless electrowetting number  $E_w$  indicates the importance of electrical energy at the solid–liquid interface relative to the interfacial energy at the liquid–fluid interface, as follows:

$$E_w = \frac{1}{\gamma_{lg}} \cdot \frac{1}{2} c_H V^2. \quad (5)$$

When Eq. (1) is introduced into the Young–Lippmann equation, the Young–Lippmann equation can be changed into an expression (6) [53].

$$\cos \theta_V = \cos \theta_0 + \frac{1}{\gamma_{lg}} \cdot \frac{\epsilon_r \epsilon_0}{2 \lambda_D} V^2, \quad (6)$$

Equation (6) shows that even if a very low voltage is applied, the droplet contact angle alteration can be sufficiently large owing to the  $\lambda_D$ . Unfortunately, due to the direct contact between conductive droplets and driving electrodes, the very low voltage can easily cause generation of electrolytes on the contact surface. In order to prevent this, an insulating layer was added on the top of the driving electrode. Adding an insulating layer gives this method an advantage over electrocapillarity and electrowetting in that it overcomes the electrolytic generation. Electrowetting-on-dielectric is a configuration in which an insulating layer separates the droplet from the driving electrodes. Finally, Eq. (6) can be revised to expression (7) [54]. The relationship between driving voltage and contact angle can be described using the revised Young–Lippmann equation.

$$\cos \theta_V - \cos \theta_0 = \frac{\epsilon_r \epsilon_0}{2 d \gamma_{lg}} V^2. \quad (7)$$

Here, driving voltage  $V$  is different from  $V$  in Eq. (2).  $V$  here is voltage drop across two layers, namely the dielectric layers and the EDL. The purpose of digital microfluidics technology is to control the droplet by charging the driving electrode under a dielectric layer, as shown in Fig. 1, and the relationship between driving voltage and contact angle can be described using Eq. (7). In its initial state, most of the droplet is located on the left

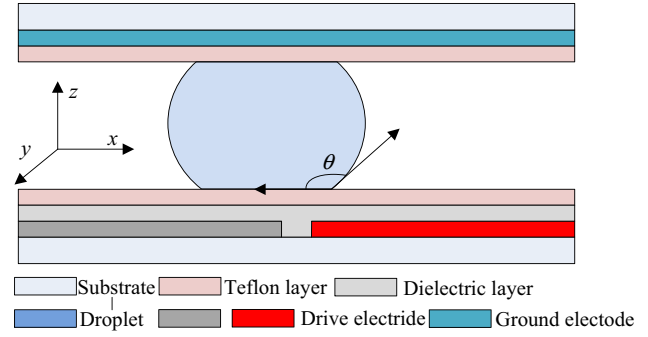


**Fig. 1** Schematic diagram of typical parallel-plate EWOD droplet actuation (side view)

side of the driving electrode, which is not charged. When the right side of the drive electrode is charged, the contact angle  $\theta$  of the droplet above the charged driving electrode decreases, and the droplet begins to move toward the charged driving electrode when the reduction in  $\theta$  is sufficiently large. If an array of driving electrodes is charged in sequence, the droplet can move along the planned path. The digital microfluidics control method includes four basic manipulations of droplet: dispensing, separation, consolidation, and transport [7–9].

### 3. Results and discussion

#### 3.1. Polarization mechanism of solid–liquid contact surface

In electromagnetics, the dielectrics exhibit electrical properties under external electric fields. There is no free charge inside the ideal insulating medium, but there is always a small amount of free charge inside the actual dielectric. These small amounts of free charge cause dielectric leakage. Under normal circumstances, in the absence of an electric field, the positive and negative charges offset each other at every point, showing no electrical properties in the macrostate. Under an external electric field, the local movement of bound charge produces electrical properties in a macrostate, showing charges on the surface of the dielectric and in the non-uniform component within the dielectric. This phenomenon is called polarization, and the charge that emerges is called the polarization charge. These charges change the original electric field. For example, the capacitance of a capacitor filled with dielectric elements is larger than that of the vacuum capacitor, due to the polarization of the dielectric. The electric dipole generated by polarization is called “induced electric dipole,” and its electric dipole moment is called “induced electric dipole moment.” Polarization intensity  $P$  is a vector: Its size is the density of electrical

dipole moment in the dielectric, that is, the electrical dipole moment per unit volume, which is also known as the polarization intensity, or polarization vector. The electric dipole moment defined here refers to both permanent electric dipole moment and induced electric dipole moment. The relationship among polarization intensity  $P$ , electric field  $E$ , and electric displacement  $D$  is expressed as follows:

$$D = \varepsilon_0 E + P = \varepsilon_0 \varepsilon_r E, \quad (8)$$

Here,  $\varepsilon_0$  is the vacuum dielectric constant, and  $\varepsilon_r$  is the relative dielectric constant of the dielectric. For isotropic and linear dielectrics, the ratio of electrodynamic intensity over electric field is the polarization ratio  $\chi_e$ :

$$P = \chi_e \varepsilon_0 E. \quad (9)$$

In this way, the electric displacement is proportional to the electric field:  $D = \varepsilon_0(1 + \chi_e)E = \varepsilon E$ , where  $\varepsilon$  is the permittivity (dielectric constant). The relationship between the relative permittivity and the electrode rate is  $\varepsilon_r = 1 + \chi_e$ .

For polarization intensity, electric field, electric displacement, and the direction of these three vectors are the same. The physical quantities described in electromagnetism are mostly mean values in macroscopic state. For example, the average magnitude of the electric field, average dipole density, and average polarization strength are considered on a much larger scale than atomic size. However, when the microscopic problem is studied, the relationship between polarization of individual particles in the dielectric apparatus, the average polarization ratio, and the average polarization intensity can be expressed using the Clausius–Mossotti equation.

$$\frac{\varepsilon_r - 1}{\varepsilon_r + 2} = \frac{1}{3\varepsilon_0} \sum_j N_j \alpha_j \quad (10)$$

Here,  $N$  is the number of molecules per unit volume,  $\alpha$  and  $j$  represent the molecular polarization ratio and the  $j$  molecule, respectively. This equation expresses the relationship between molecular polarization and dielectric constant. The equation establishes a connection between microscopic parameter (polarizability) and macroscopic parameter (dielectric constant), which is the bridge connecting the microscopic and macroscopic worlds. The equation is beneficial to understanding the intrinsic nature of dielectrics at molecular level, specifically, the mechanism of the solid–liquid contact surface under electric field.

In the EWOD chip shown in Fig. 2, the electric dipole and free charge in the droplet are randomly distributed in the droplet when the right gray driving electrode is not charging, as shown in Fig. 2(a). When the right gray electrode is charging and turning red, an electric field

forms between the driving electrode and zero electrode, as shown in Fig. 2(b). Under the electric field, a large positive charge accumulates on the surface of the hydrophobic layer and becomes the surface-bound charge. Under the effect of this surface-bound charge, the negatively charged free charge and the negatively charged portion of droplet near the surface of bound charge are drawn to the surface due to attractive force between opposite charges. Macroscopically, the hydrophobic layer of droplets located above the conductive driving electrode exhibits hydrophilicity, and the contact angle of droplet above the portion is reduced. In this process, droplets are subject to electrostatic forces, and the electrostatic force is the main cause of the change in the contact angle of the droplets.

### 3.2. EWOD drive force characterization

The relevant model parameters are shown in Table 1. In the numerical simulation, the droplet can be regarded as dielectric [14, 20, 21].

The applied voltage generates an electrostatic field in the vicinity of the droplet, and the EWOD driving force component caused by the electric field is represented by Eq. (11):

$$F_i = \iint \sum_{j=1}^3 T_{ij} ds_j, \quad (11)$$

Here,  $s_j$  represents the per unit area of the  $j$ th coordinate direction in the direction of  $i$ th coordinate direction. From tensor operation rule, it is known for each Maxwell stress tensor element, and the following is true:

$$T_{ij} = \varepsilon(E_i E_j - \frac{1}{2} \delta_{ij} E^2), \quad (12)$$

Here,  $E_i$  represents the electric field intensity of the  $i$ th coordinate direction in the space perpendicular coordinate system, and  $\delta_{ij}$  is the Kronecker function,

$$\delta_{ij} = \begin{cases} 1 & \dots \dots i = j \\ 0 & \dots \dots i \neq j \end{cases}$$

Based on the Gauss theorem, the loop Maxwell stress tensor can be obtained as follows:

$$T = \varepsilon(\vec{E} \vec{E} - \frac{1}{2} I \cdot E^2), \quad (13)$$

Here,  $I$  is the second-order unit tensor,  $\vec{E}$  is the electric field intensity:  $E^2 = E_x^2 + E_y^2 + E_z^2$ , and  $\varepsilon$  is the dielectric constant of the droplet.

The Maxwell stress tensor is rewritten in matrix form as follows:

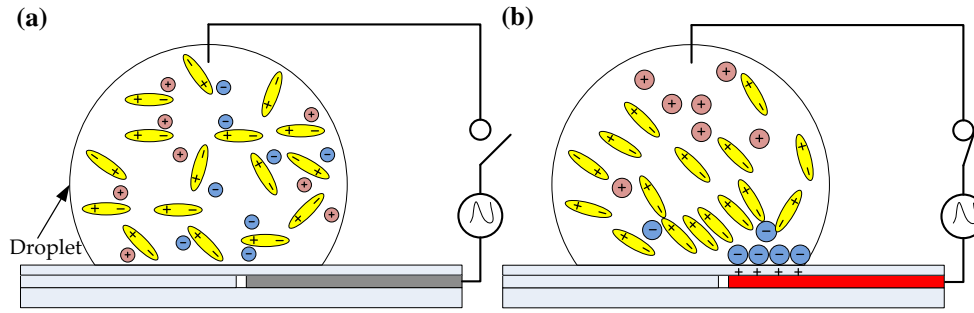


**Fig. 2** Schematic diagram of the change in charge and electric dipole in the droplet before and after the application of the electric field (side view): (a) before the electric field is brought to bear, and (b) after the electric field is brought to bear

**Table 1** Parameters used in numerical simulation

Parameter	Value
Electrode dimensions ( $L \times L$ )	$1 \times 1 \text{ mm}^2$
Electrode spacing ( $g$ )	$20 \text{ }\mu\text{m}$
Dielectric layer thickness ( $d$ )	$2 \text{ }\mu\text{m}$
Droplet volume	$1 \text{ }\mu\text{L}$
Droplet radius ( $R$ )	$702 \text{ }\mu\text{m}$
Droplet base radius	$680 \text{ }\mu\text{m}$
Static contact angle ( $\theta_0$ )	$118^\circ$
Droplet conductivity ( $\sigma$ )	$5.5 \times 10^{-6} \text{ S/m}$
Relative permittivity of droplet ( $\epsilon_d$ )	80
Relative permittivity of dielectric ( $\epsilon_r$ )	3.2
Relative permittivity of air ( $\epsilon_0$ )	1
Actuation voltage ( $V$ )	$100 \text{ Vrms}$
Plate gap ( $h$ )	$1000 \text{ }\mu\text{m}$

$$T = \epsilon \cdot \begin{bmatrix} \frac{(E_x^2 - E_y^2 - E_z^2)}{2} & \dots & E_x E_y & \dots & E_x E_z \\ \dots & E_x E_y & \dots & \frac{(E_y^2 - E_x^2 - E_z^2)}{2} & \dots & E_y E_z \\ \dots & E_x E_z & \dots & E_y E_z & \dots & \frac{(E_z^2 - E_x^2 - E_y^2)}{2} \end{bmatrix} \quad (14)$$

Using the Gauss theorem, we can obtain the EWOD driving force in the  $x$ ,  $y$ , and  $z$  directions for the droplet in Fig. 1.

$$\begin{cases} F_x = \epsilon \iiint \sum \left[ \frac{d}{dx} \left( \frac{E_x^2 - E_y^2 - E_z^2}{2} \right) + \frac{d}{dy} (E_x E_y) + \frac{d}{dz} (E_x E_z) \right] dv \\ F_y = \epsilon \iiint \sum \left[ \frac{d}{dx} (E_x E_y) + \frac{d}{dy} \left( \frac{E_y^2 - E_x^2 - E_z^2}{2} \right) + \frac{d}{dz} (E_y E_z) \right] dv \\ F_z = \epsilon \iiint \sum \left[ \frac{d}{dx} (E_x E_z) + \frac{d}{dy} (E_y E_z) + \frac{d}{dz} \left( \frac{E_z^2 - E_x^2 - E_y^2}{2} \right) \right] dv \end{cases} \quad (15)$$

Because the EWOD driving force along  $y$  and  $z$  direction has a weak and negligible effect on droplet movement, the EWOD drive force on the droplet can be simplified as follows:

$$F_x = \epsilon \iiint \sum \left[ \frac{d}{dx} \left( \frac{E_x^2 - E_y^2 - E_z^2}{2} \right) + \frac{d}{dy} (E_x E_y) + \frac{d}{dz} (E_x E_z) \right] dv. \quad (16)$$

Figure 3 shows a “droplet, driving electrode, dielectric layer, and medium” system. This figure shows the three-dimensional model after discretizing. For the sake of simplification, the numerical simulation selects only the

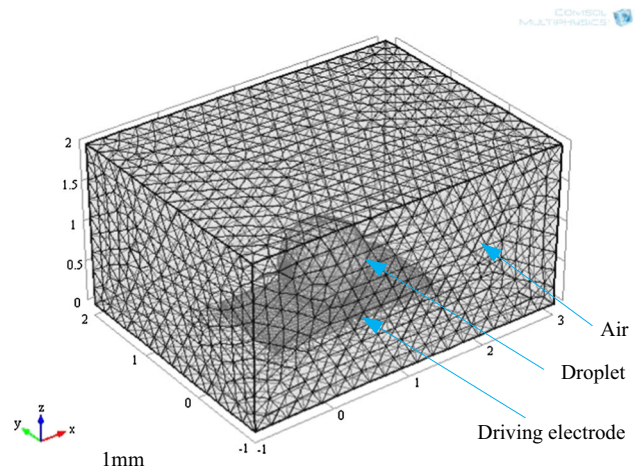


**Fig. 3** Three-dimensional simulation model of droplet (scale bar: 1 mm)



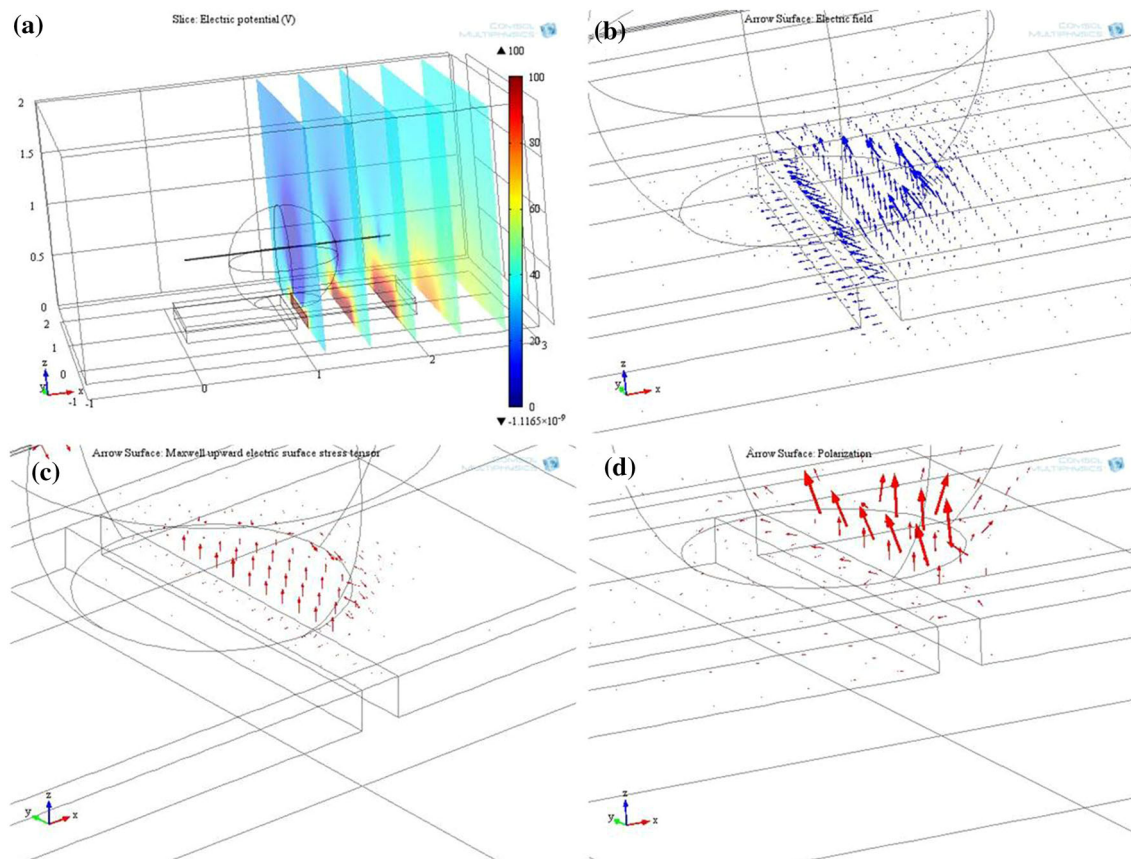
left and right driving electrodes, and air serves as the medium.

Figure 4(a) shows the potential profile when the right-side driving electrode is turned on. In order to better indicate the potential profile after the driving electrode is turned on, the slice mode is selected during post-processing. Apparently, the potential on the right drive electrode is close to 100 V. Figure 4(b) shows the electric field distribution of the solid–liquid contact surface. The density and size of the arrow indicate the size of the electric field at that point. It is clear that the electric field is strongest along the cross section of the droplet on the right driving electrode, showing a concentrated distribution. The direction of electric field points to the zero electrode. Figure 4(c) shows the distribution of Maxwell stress tensor on solid–liquid contact surface. The density of arrows indicates the size of Maxwell stress tensor, and it is readily visible that Maxwell stress tensors are the densest and largest on the right side of the driving electrode that is conducting.

According to Maxwell's theory, the electric field serves as the bridge for the transmission of force, and the coulombic force produced by charge is transmitted by the electric field. After the driving electrode is turned on and

electric field forms, the total electric field distribution is calculated and the Maxwell stress tensor then can be elicited. According to Eq. (16) above, the Maxwell stress tensor serves as a bridge to calculate the EWOD driving force applied on droplet in the EWOD chip. When the Maxwell stress tensor is calculated, the EWOD drive force can be found. Similarly, Fig. 4(c) shows the Maxwell stress tensor of a droplet on the solid–liquid interface with arrows. This was confirmed in the preceding article via theoretical analysis of the electrostatic force.

Figure 4(d) is a numerical simulation of polarization effect on the surface of driving electrode. Under the effect of the electric field, objects with opposite charges tend to attract each other. Inside an EWOD chip system, there is at first no electric dipole moment between dielectric materials and molecules in droplets. In the presence of an external electric field, however, relative displacement of positive and negative charges occurs, so they form electric dipoles with a certain torque along the direction of external electric field. On the solid–liquid interface, there are positive and negative surface-bound charges. The arrow in Fig. 4(d) indicates the abstract concept of polarization, where larger arrows are centered within the circle of



**Fig. 4** Simulation results of electrical field: (a) potential distribution of EWOD chip, (b) electric field distribution of solid–liquid contact surface, (c) Maxwell stress tensor distribution of solid–liquid contact surface, and (d) polarization map of solid–liquid contact surface

droplet, indicating that the polarization effect is present in this area. Figure 4(d) is consistent with the aforementioned content. First, the solid–liquid interface is located above the conducting driving electrode and generates a polarization effect under the effect of electric field. In this process, the droplet is subject to electrostatic force; second, there are changes in the surface-bound charge in this part of solid–liquid contact surface, disrupting the balance of surface tension at the surface of the droplet; finally, the unbalanced surface tension causes the droplet to deform to an extent, and the deformation of the droplet exacerbates the difference in pressure inside the droplet, which causes the droplet to move.

### 3.3. Discussion of pressure field and flow field

During the simulation process, the evaporation, contact angle saturation, and hysteresis of the droplets are neglected. Figure 5 which is a  $y = 0$  plane view shows the results of numerical simulation of the hydrostatic pressure inside the droplet. Figure 5(a) through Fig. 5(d) shows the changes in pressure inside the droplet at different times. Figure 5(a) shows the pressure inside the droplet at the initial time. Because an electric field is formed between the upper and lower plates of the chip when the right driving electrode is turned on, the droplet undergoes a certain amount of deformation in response to electrostatic force and surface tension.

Then, the deformation creates a hydrostatic pressure gradient inside the droplet. At this time, the hydrostatic pressure of the forward part of the droplet is larger than that of other parts of the droplet. Figure 5(b) shows that the part of the droplet with the highest internal pressure begins to move upward toward the surface of the droplet as driving time continues. As shown in Fig. 5(c), the part with the highest internal pressure continues to move to the left and reaches the left side of the droplet, and then, it begins to expand as driving time continues. As shown in Fig. 5(d), this part of the droplet moves into the rest of the droplet as the driving time ends and continues to expand. The droplet moves to the right under its internal hydrostatic pressure gradient.

Figure 6 shows the results of numerical simulation of internal flow field of droplet. In Fig. 6(a), part of the droplet begins to advance; in Fig. 6(b), the part of the droplet that is advancing continues to move to the right, and the droplet undergoes a certain amount of deformation, indicating that the part of the droplet with the highest internal pressure moved to the left; in Fig. 6(c), the advancing part of the droplet continues to move to the right. The droplet in Fig. 6(c) is more deformed than in Fig. 6(b), indicating that the part of the droplet with the largest internal pressure is increasing in size and is concentrated on the left side of the

droplet. In Fig. 6(d), the advancing part of the droplet continues to move to the right, and the entire droplet, including the rest of the droplet, begins to move, indicating that the droplet begins to move under the force of the difference in its own internal hydrostatic pressure. In this way, droplets are driven from one point to another.

Figure 5 illustrates the process by which the difference in hydrostatic pressure is generated within the droplet. Figure 6 shows the variation in the internal flow field of the droplet corresponding to the difference in hydrostatic pressure. The two figures together show that under the difference in internal hydrostatic pressure, the droplet first undergoes a certain amount of deformation; then, the portion with the highest pressure starts to move within the droplet, and finally, the rest of the droplet moves. Corresponding to the generation and movement of the difference in hydrostatic pressure, the droplet will be deformed. As the maximum pressure moves to the rest of the droplet and the portion expands, the deformation of the droplet increases. When the difference in hydrostatic pressure is large enough, the droplets will be driven successfully.

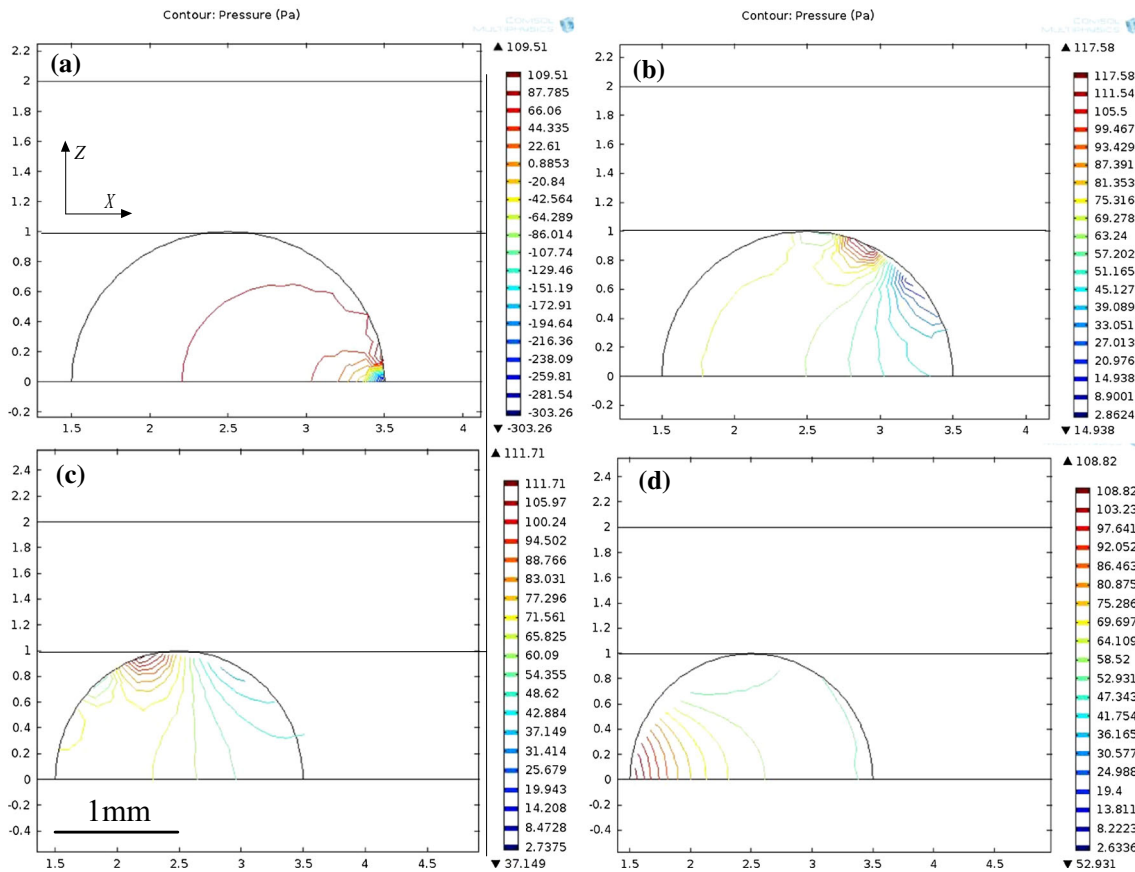
### 3.4. Transition from stillness to motion

Figure 7 shows schematic side views of EWOD chip and droplet geometry. According to the Laplace–Young equation, the difference in hydrostatic pressure [13, 41] between point 1 and point 2 within the droplet is given as follows:

$$P_1 - P_2 = \gamma_{lg} \left[ \left( \frac{1}{r_1} - \frac{1}{r_2} \right) + \left( \frac{1}{R_1} - \frac{1}{R_2} \right) \right]. \quad (17)$$

Here,  $\gamma_1$  and  $\gamma_2$  indicate the radius of curvature of the rest of the droplet and the advancing part of the droplet, respectively,  $R_1$  and  $R_2$  denote the radius of the rest of the droplet and the advancing portion of the droplet, respectively, and  $p_a$  indicates the air pressure. As shown in Fig. 7(a), the parts of droplet inside the No. 1 and No. 2 dashed rectangles represent the rest of the droplet and the advancing part of the droplet, respectively. Thereinto, point 1 and point 2 are two symmetric random points before the driving voltage is applied. These are located on the part of droplet represented by dashed rectangles 1 and 2.

As shown in Fig. 7(a), the radius of curvature of rest of the droplet is smaller than the radius of curvature of advancing portion of the droplet, that is,  $\gamma_1 < \gamma_2$ . The radius of the rest of the droplet is smaller than the curvature of the advancing part of the droplet, that is,  $R_1 < R_2$ . In this way, the sum of the differences in pressure at each point in the rest of the droplet and advancing portion of the droplet is approximately equal to the difference in total hydrostatic pressure inside the droplet:  $\Delta P = \sum_{i=1}^n P_i$ , in which  $P_i \approx P_1 - P_2$  here, and  $n$  represents a random point in either the rest of the droplet or the advancing part of droplet. The



**Fig. 5** Numerical simulation of the internal pressure of droplets at different times: (a) time = 0.005 s, (b) time = 0.009 s, (c) time = 0.015 s, and (d) time = 0.02 s

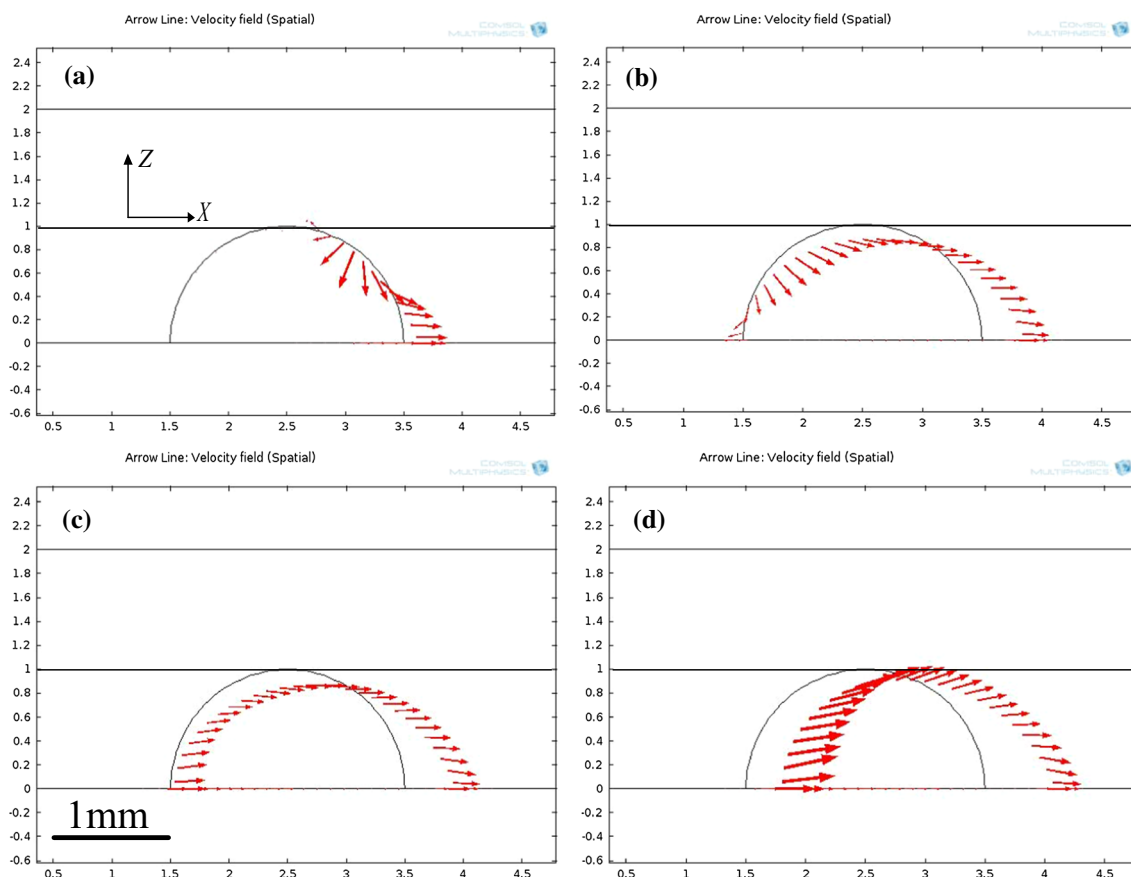
calculation of the difference in pressure disregards the contact angle hysteresis of droplets and the viscous resistance of surrounding media to the droplet. It is an ideal mathematical model.

Figure 7(b) shows the transport of maximum pressure region inside the droplet along with the driving time. Four circles labeled 1–4 represent the areas of maximum pressure inside the droplet at different times. The area within the circle represents the size of the area of maximum pressure. As mentioned earlier, as driving time continues, the maximum pressure region rotates within four locations from 1 to 4. At this time, the area is continuously increasing in size. The region of maximum pressure no longer moves when it moves to the location of circle 4 but rather remains at this position and increases in area. At this moment, hydrostatic pressure  $\Delta P$  is generated inside the droplet, which drives the movement of the droplet toward the direction with lower pressure when  $\Delta P$  is large enough. According to the literature of free-body representation, the surface tension component of gas–liquid interface in direction is  $F_x = \gamma_{lg} \cos \theta_V$  [50]. Based on the above analysis, the EWOD driving force, surface tension, and

fluid static pressure are approximately equal to each other, i.e.,  $F_x \approx \gamma_{lg} \cdot \cos \theta \approx \Delta P$ .

As the droplet moves from stillness to motion, the free charge and the electric dipole inside the droplet under electric field are drawn to the surface-bound-charge in the water-repellant layer of the chip. This process renders the hydrophobic layer hydrophilic. As the wettability of the hydrophobic layer increases, the corresponding part of the droplet can spread out, and the contact angle of this part of the droplet decreases. The spreading part of the droplet is undergoing forward movement, in which static force takes on a dominant role, and the droplet as a whole is subject to a EWOD drive force. Then, the different shapes of the surfaces of the advance and recovery parts of droplet will cause the droplet to deform. The deformation can break the balance of surface tension. At this time, the contact angle change of the remainder of the droplet is very small and can be disregarded. The surface tension is dominant, and the droplet is subject to surface tension  $F_x \approx \gamma_{lg} \cdot \cos \theta$ . Next, the hydrostatic pressure of the remainder of the droplet is greater than that of advancing portion, and the imbalance in surface tension can disrupt the balance of





**Fig. 6** Numerical simulation of droplet flow field at different times: (a) time = 0.009 s, (b) time = 0.015 s, (c) = 0.02 s, and (d) time = 0.025 s

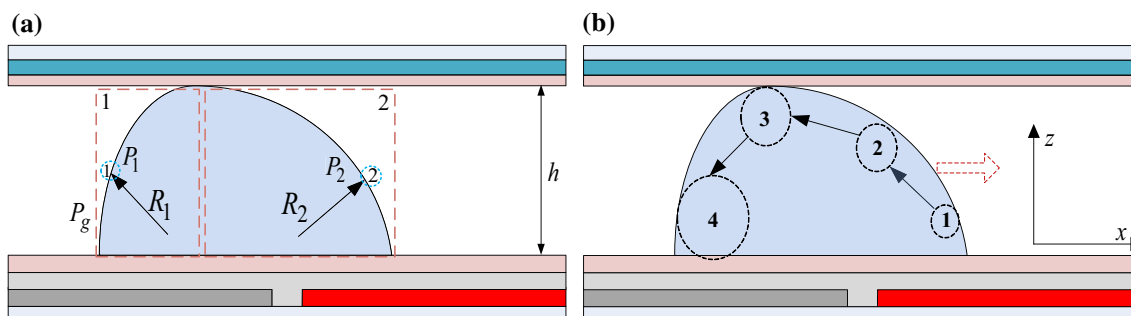


**Fig. 7** (a) EWOD chip and droplet geometry diagram, and (b) changes in the internal pressure of the droplet and diagram of maximum pressure area (side view)

pressure within the droplet. This generates static pressure inside the droplet, i.e., the hydrostatic pressure comes to bear on the drop such that the droplet can be successfully driven by sufficiently large hydrostatic pressure.

### 3.5. Experimental verification

To validate the manner of droplet transitions from stillness to motion, two EWOD chip structures were fabricated and

assembled. The main fabrication process and the experimental setup are listed in our recent work [21]. The devices had layers with a thickness of 2 μm and 50 nm for SU8 and Teflon, respectively. During the experiment, double-sided adhesive tapes were used to secure the upper and lower plates of the chip, with an inter-plate spacing of 300 μm. The suspended wire or the upper plate is connected to the null electrodes. The drive electrodes were connected to a sinusoidal signal of frequency 100 Hz and magnified

through a voltage amplifier circuit. Deionized water droplets were used, and medium for droplet manipulation was air. The transition of the droplet was recorded from the top using a high-speed camera attached to an optical microscope on a vibration isolation table. The droplet velocity was obtained by analyzing the recorded video clips according to Fig. 8, which are the time-lapse CCD images of a 1  $\mu\text{l}$  droplet. Calculations then showed that the average speed of the 1  $\mu\text{l}$  droplet [13, 45] in air medium reaches approximately 170 mm/s and 120 mm/s when the supply voltage is 40 Vrms.

Because ITO glass has good transparency, but turns opaque after coated with the SU-8 photoresist layer, in the video frame images of droplet motion, the contours of the drive electrodes were outlined with dashed boxes, and the droplet moves from left to right in the electrode array, as shown in Fig. 8. As depicted in Fig. 8(a), 1  $\mu\text{l}$  deionized droplet is driven in EWOD chip with suspended wire as the zero electrode, and Fig. 8(b) shows that the 1  $\mu\text{l}$  droplet is driven in EWOD chip with upper zero plate. The droplets move from left to right in the electrode array as shown in Fig. 8(a) and (b). The droplet transitions in Fig. 8 indicate that two chip structures, no matter what those structures may be, cause the droplet to transition from stillness to motion in the same way. As shown in Fig. 8, the part of the first droplet that is advancing is on the charged electrode, and the rest of the droplet above the uncharged electrode retains its original shape. In this process, the asymmetrical

change in the droplet shape causes a certain amount of droplet deformation. On this account, within the droplet, the asymmetrical deformation produces a difference in hydrostatic pressure, and when this difference in hydrostatic pressure is sufficiently large, the droplet can be successfully driven from stillness to motion. As exhibited in Fig. 8(a) and (b), an array of driving electrodes is charged in sequence, and the droplet can move along the planned path, as shown in images 1 through 4.

In summary, according to the analysis and experiment results mentioned above, the process from stillness to motion needs to go through the following four successive steps:

Step 1: The “EWOD chip–droplet” can be considered as a capacitive system. When the driving electrode is turned on, the contact angle of the droplet above the conductive driving electrode decreases.

Step 2: The decrease in the contact angle changes the surface tension of the droplet, while the contact angle of droplet above the non-conducting electrode retains its initial contact angle, and the surface tension remains constant.

Step 3: The asymmetrical change in the surface tension of the droplets causes a certain amount of deformation of the droplet.

Step 4: The deformation of the droplet produces a difference in hydrostatic pressure within the droplet, and the droplet can be successfully driven when this difference in hydrostatic pressure is sufficiently large.

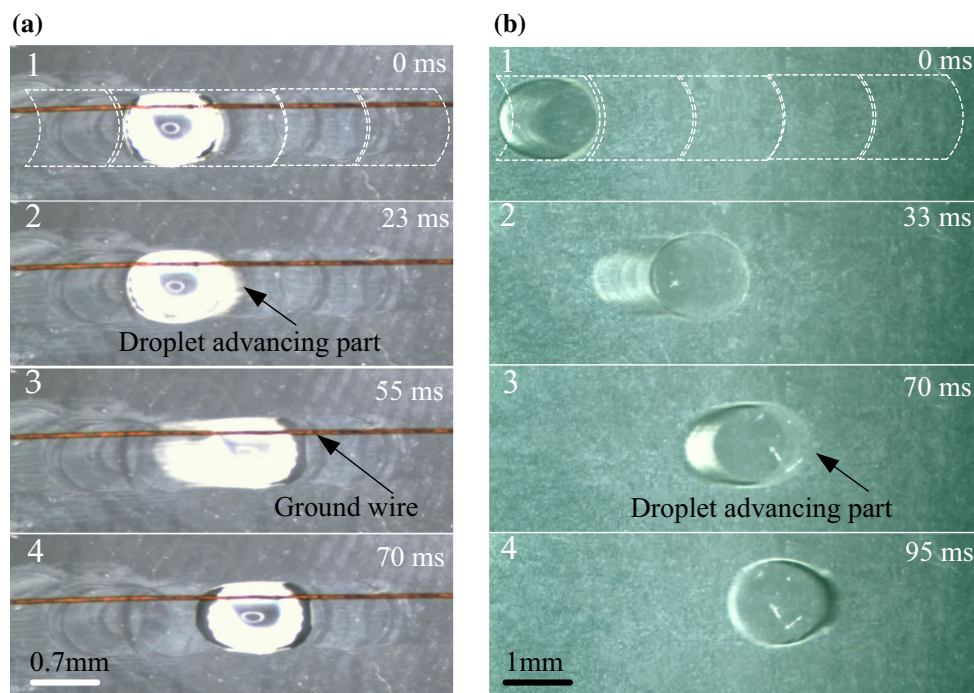


**Fig. 8** Transition of a 1  $\mu\text{l}$  droplet under an AC voltage 40 Vrms and frequency 100 Hz: (a) the ground electrode is suspended zero wire, and (b) the ground electrode is upper zero plate (top view)

#### 4. Conclusions

In summary, we studied the mechanism underlying the bound charge of the solid–liquid interface. Then, the electric field, pressure field, and flow field in the EWOD chip–droplet system were simulated. The results and discussion of numerical simulation showed that, in the presence of the electric field, the positive and negative ions and molecules attracted each other to bring an electrostatic force to bear on the solid–liquid contact surface. The electrostatic force changed the surface tension of the droplets, causing different levels of surface tension on the left and right sides of the droplets and leading to droplet deformation. The deformation generated a difference in hydrostatic pressure within the droplet. Finally, a sufficiently large difference in hydrostatic pressure could successfully drive the droplets from rest to motion. Most importantly, the experimental observations are consistent with the predicted droplet asymmetrical deformation owing to the asymmetrical change in the surface tension. We here explained the process of droplet transitions from stillness to motion, and analyzed the mechanism by which droplets may be successfully driven, providing a theoretical basis for a better understanding and use of digital microfluidics technology. However, in our work, many other elements, including the contact angle saturation effects, the contact angle hysteresis effects, and the ion flux/transport effects, are disregarded. Our further work will focus on the effects of these factors in EWOD mechanism for the movement of the droplet.

**Acknowledgements** This work was supported in part by the Zhejiang Provincial Natural Science Foundation of China (Grant No. LQ16E050008), the Key Laboratory of Air-driven Equipment Technology of Zhejiang Province (Grant No. 2018E10011), and the National Natural Science Foundation of China (Grant No. 51275327).

#### References

- [1] M Abdelgawad and A R Wheeler *Adv. Mater.* **21** 920 (2010)
- [2] K Choi, A H C Ng, R Fobel and A R Wheeler *Annu. Rev. Anal. Chem.* **5** 413 (2012)
- [3] J L He, A T Chen, J H Lee and S K Fan *Int. J. Mol. Sci.* **16** 22319 (2015)
- [4] Y H Yu, J F Chen and J Zhou *J. Micromech. Microeng.* **24** 015020 (2014)
- [5] H H Shen, S K Fan, C J Kim and D J Yao *Microfluid. Nanofluid.* **16** 965 (2014)
- [6] S Chen, M R Javed, H K Kim, J Lei, M Lazari, G J Shah, R M V Dam, P Y Keng and C J Kim *Lab Chip* **14** 902 (2014)
- [7] J H Song, R Evans, Y Y Lin, B N Hsu and R B Fair *Microfluid. Nanofluid.* **7** 75 (2009)
- [8] M Abdelgawad, P Park and A R Wheeler *J. Appl. Phys.* **105** 094506 (2009)
- [9] J Gong and C J Kim *Lab Chip* **8** 898 (2008)
- [10] Y Li, Y Q Fu, S D Brodie, M Alghane and A J Walton *Biomicrofluidics* **6** 12812 (2012)
- [11] D G Pyne, W M Salman, M Abdelgawad and Y Sun *Appl. Phys. Lett.* **103** 70 (2013)
- [12] T Chen, C Dong, J Gao, Y Jia, P I Mark, M I Vai and R P Martins *AIP Adv.* **4** 047129 (2014)
- [13] S K Cho, H Moon and C J Kim *J. Microelectromech. S.* **12** 70 (2003)
- [14] S W Walker and B Shapiro *J. Microelectromech. S.* **15** 986 (2006)
- [15] J Chen, J Yu, J Li, Y Lai and J Zhou *J. Appl. Phys. Lett.* **101** 245 (2012)
- [16] V Jain, T P Raj, R Deshmukh and R Patrikar *Microsyst. Technol.* **21** 1 (2015)
- [17] A C Madison, M W Royal and R B Fair *J. Microelectromech. S.* **25** 593 (2016)
- [18] Y Li, R J Baker and D Raad *Actuat. B-Chem.* **229** 63 (2016)
- [19] C P Lee, H C Chen and M F Lai *Biomicrofluidics* **6** 12814 (2012)
- [20] A Ahmadi, J F Holzman, H Najjarian and M Hoorfar *Microfluid. Nanofluid.* **10** 1019 (2011)
- [21] X Xu, L Sun, L Chen, Z Zhou, J Xiao and Y Zhang *Biomicrofluidics* **8** 064107 (2014)
- [22] H H Shen, L Y Chung and D J Yao *Biomicrofluidics* **9** 022403 (2015)
- [23] D S Wang, and S K Fan *Sensors* **16** 1175 (2016)
- [24] K Chakrabaty, R B Fair and J Zeng *IEEE T. Comput. Aid. D.* **29** 1001 (2010)
- [25] M J Jebraill, M S Bartsch and K D Patel *Lab Chip* **12** 2452 (2012)
- [26] Z Zeng, K Zhang, W Wang, W Xu and J Zhou *IEEE Sens. J.* **16** 4531 (2015)
- [27] N Vergauwe, D Witters, F Ceysens, S Vermeir, B Verbruggen, R Puers and J Lammertyn *J. Micromech. Microeng.* **21** 054026 (2011)
- [28] S M George and H Moon *Biomicrofluidics* **9** 024116 (2015)
- [29] A H C Ng, M D Chamberlain, H Situ, V Lee and A R Wheeler *Nat Commun* **6** 7513 (2015)
- [30] P Y Hung, P S Jiang, E F Lee, S K Fan and Y W Lu *Microsyst. Technol.* **1** (2015)
- [31] D J Yao *J. Adhes. Sci. Technol.* **26** 1 (2012)
- [32] M G Pollack, V K Pamula, V Srinivasan and A E Eckhardt *Expert. Rev. Mol. Diagn.* **11** 393 (2011)
- [33] A E Kirby and A R Wheeler *Lab Chip* **13** 2533 (2013)
- [34] E Y Basova and F Foret *Analyst* **140** 22 (2015)
- [35] H Y Huang, H H Shen, C H Tien, C J Li, S K Fan, C H Liu, W S Hsu and D J Yao *Plos One* **10**, e0124196 (2015)
- [36] Z Zhang, C Hitchcock and R F Katlicek *Appl. Optics.* **55** 9113 (2016)
- [37] S Y Park and Y Nam *Micromachines* **8** 3 (2016)
- [38] A Tröls, S Clara and B Jakoby *Actuat. A-Phys.* **244** 261 (2016)
- [39] E Baird, P Young and K Monseni *Microfluid. Nanofluid.* **3** 635 (2007)
- [40] R Bavière, J Boutet and Y Fouillet *Microfluid. Nanofluid.* **4** 287 (2008)
- [41] D Chatterjee, H Shepherd and R L Garell *Lab Chip* **9** 1219 (2009)
- [42] S Choi, Y Kwon and J Lee *Appl. Phys. Lett.* **105** 183509 (2014)
- [43] K Adamiak *Microfluid. Nanofluid.* **2** 471 (2006)
- [44] N Kumari, V Bahadur and S V Garimella *J. Micromech. Microeng.* **18** 105015 (2008)
- [45] J K Park, S J Lee and K H Kang *Biomicrofluidics* **4** 024102 (2010)
- [46] J K Park and K H Kang *Phys. Fluids* **24** 042105 (2012)
- [47] H Lee, S Yun, S H Ko and K H Kang *Biomicrofluidics* **3** 44113 (2009)

- 
- [48] M J Schertzer, S I Gubarenko, R Ben-Mrad and P E Sullivan *Langmuir* **26** 19230 (2010)
- [49] W Cui, M Zhang, X Duan, W Pang, D Zhang and H Zhang *Micromachines* **6** 778 (2015)
- [50] W C Nelson and C J Kim *J. Adhes. Sci. Technol.* **26** 1747 (2012)
- [51] F Mugele and J C Baret *J. Phys-Condens. Mat* **17** R705 (2005)
- [52] M Ammam, D D Caprio and L Gaillon *Electrochim. Acta* **61** 207 (2012)
- [53] D Beyssen, L L Brizoual, O Elmazria and P Alnot *Sens Actuator B* **118** 380 (2006)
- [54] J Y Y And and R L Garrell *Anal. Chem.* **75** 5097 (2003)